Supporting Information

Blister Test to Measure the Out-of-Plane Shear Modulus of Few-Layer Graphene

Metehan Calis[1], Narasimha Boddeti[2], and J. Scott Bunch[1,3*]

[1]Boston University, Department of Mechanical Engineering, Boston, MA 02215 USA

[2]Washington State University, School of Mechanical and Materials Engineering, Pullman, WA 99163 USA

[3]Boston University, Division of Materials Science and Engineering, Brookline, MA 02446 USA

*e-mail: bunch@bu.edu

1. Growth and Characterization

We grow monolayer MoS_2 flakes using chemical vapor deposition (CVD). First, a SiO_x wafer is cleaned with acetone, isopropyl alcohol (IPA), and deionized water (DI) and exposed to ultraviolet (UV) light for 5 minutes. MoS_2 powder (Thermo Fisher Scientific, Molybdenum (IV) sulfide, 98%) is positioned in the middle of a furnace and a SiO_x wafer is placed into a cooler region downstream (~ 650 – 700 ^oC). The furnace is purged with argon (200 sccm) to remove air quickly and make the furnace an argon-rich environment. Then the furnace is placed under vacuum and 60 sccm Ar, 0.06 sccm O_2, and 1.8 sccm H_2 are introduced inside the tube. The growth process consists of three steps: (i) heating up to 900 ^oC for 15 minutes, (ii) holding at 900 ^oC for 15 minutes, and (iii) cooling the furnace to room temperature.

Using optical contrast[1], Raman spectroscopy and photoluminescence (PL) spectroscopy, we identify monolayer MoS_2 flakes. Both Raman and PL spectroscopy were conducted in a Renishaw Raman InVia microscope using a 532 nm laser beam with 1200 I/mm gratings. The in-plane (E^1_{2g}) and out-of-plane (A_{1g}) vibrations located at 385 cm^{-1} and 405 cm^{-1} respectively[2] in Raman spectrum, and A exciton peak[3] in the PL spectrum located at 1.88 eV show that the membranes are single layered.

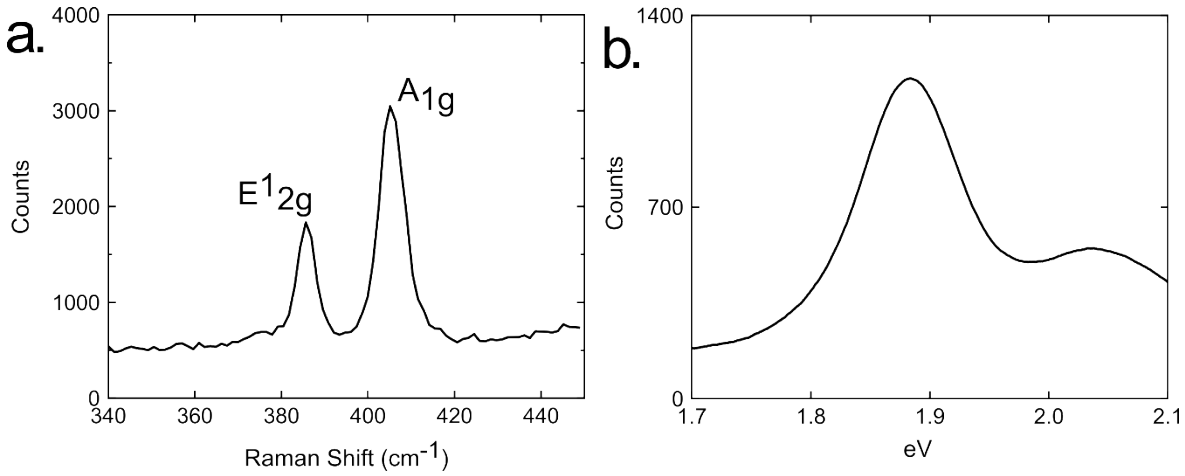

Figure S1. a) Raman spectrum. **b)** PL spectrum.

2. Graphite Substrate Fabrication and MoS_2 layers transfer

We start with cleaning the SiO_x surface with acetone, IPA, and DI water. Utilizing the 'Scotch-Tape' method, we exfoliate the graphite flakes onto the SiO_x surface by peeling off very slowly (~ 1 mm/min). Then, the graphite-covered substrate is spin-coated with photoresist S1818 at 2500 rpm and kept on the hot plate at 115 ^oC for 1 minute. We pattern 5 μm diameter circles onto the spin-coated chips by exposing them to UV light for 20 seconds at 8 mW power. MF-319 developer is used to remove the exposed photoresist. Reactive-Ion-Etching (RIE), with parameters 3.1 sccm O_2 and 25 sccm CF_4 at 100 mTorr pressure and 150 W power for 10 minutes is used to etch through graphite, SiO_x, and Si and create wells with a depth between ~480 – 700 nm. To remove the photoresist top surface, we keep the prepared chips in a bath of 1165 Remover for 12 hours at 110 ^oC, followed by exposure to O_2 plasma to remove any remaining photoresist (Fig. S2).

Before MoS_2 transfer, we locate few-layer graphene (FLG) wells using optical contrast and AFM scans. Subsequently, we begin spin coating the CVD-grown MoS_2 flakes with PMMA at 1800 rpm. We create a window on thermal-release tape, and it is stamped onto the PMMA-covered MoS_2 substrate. We place the PMMA-covered MoS_2 substrate into DI water and let the water separate the MoS_2 flakes from the SiO_x resulting in an MoS_2/PMMA/thermal-release-tape (MPT) combination. We use a custom-made apparatus, to transfer the MPT combination over the etched wells, which has two main parts: a heating stage which helps adhere MoS_2 onto FLG wells, and a micro-manipulatable lever which allow steady approach to the FLG surface while lowering the MPT to adhere. The whole transfer process is carried out under an optical microscope and a heated (~ 85 ^oC) stage. With the help of the heat, the thermal-release-tape is peeled off easily and the MoS_2/PMMA sticks to the graphite wells. To ensure there is no trapped air inside the microcavities (resulting from the transfer process), we place them in a desiccator for a period of 12 hours. This step is carried out prior to annealing in order to prevent any potential damage that could occur during the annealing process, which takes place under vacuum condition. To remove the PMMA from the surface, we anneal the device for 7 hours at 350 ^oC under 20 sccm of argon flow.

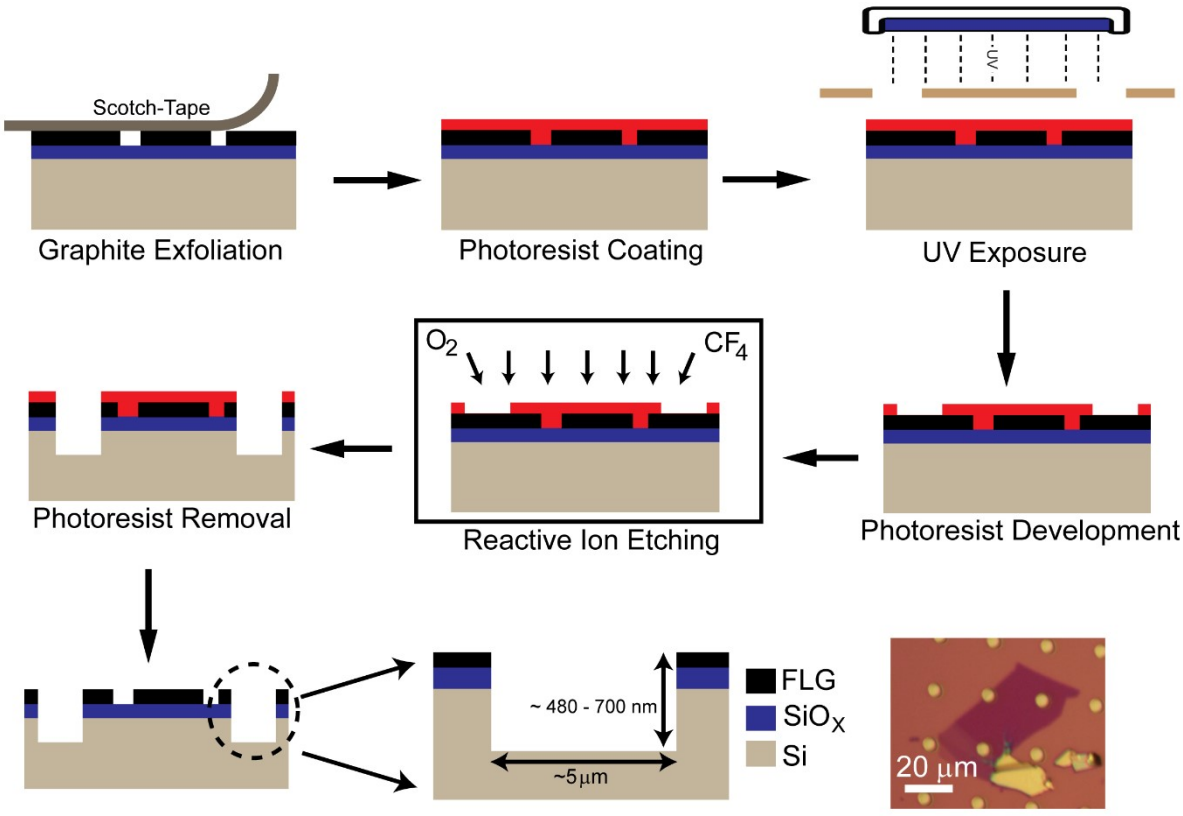

Figure S2. Microfabrication of the few-layer graphene wells.

3. Young's Modulus Calculation

To determine the Young's modulus of MoS_2, we use Hencky's solution [4–6] for the deformation of a pressurized clamped axisymmetric membrane, which relates the pressure difference (p) to deflection (δ) and radius (a) through the formula:

$$p = \frac{K(v)E_{2D}\,\delta^3}{a^4} \quad \text{(S3.1)}$$

where E_{2D} is the two-dimensional Young's modulus, a is the cavity radius, and $K(v)$ is a constant which depends on the Poisson's ratio (for MoS_2, we use $K(v = 0.29) = 3.54$).[7] From Hencky's solution, the volume under the bulge is determined by the formula $V_b = C(v)\pi a^2\delta$ where (for MoS_2, we use $C(v = 0.29) = 0.552$) and the ideal gas law ($p_0V_0 = p_{int}(V_0+V_b)$) is employed to determine p_{int}. For each input pressure, we measure δ and a of each bulge with the AFM. Using Eqn. S3.1, a linear fit to the data is used to determine E_{2D} for each device (Fig. S3a). The values of E_{2D} are consistent with monolayer MoS_2 (Fig. S3b). The variation in the E_{2D} values observed in the CVD-grown MoS_2 membranes can be attributed to sulfur vacancies[8,9], varying densities of defects[10] resulting from different growth conditions, and introducing strain[11] over the MoS_2 membrane due to the transfer process.

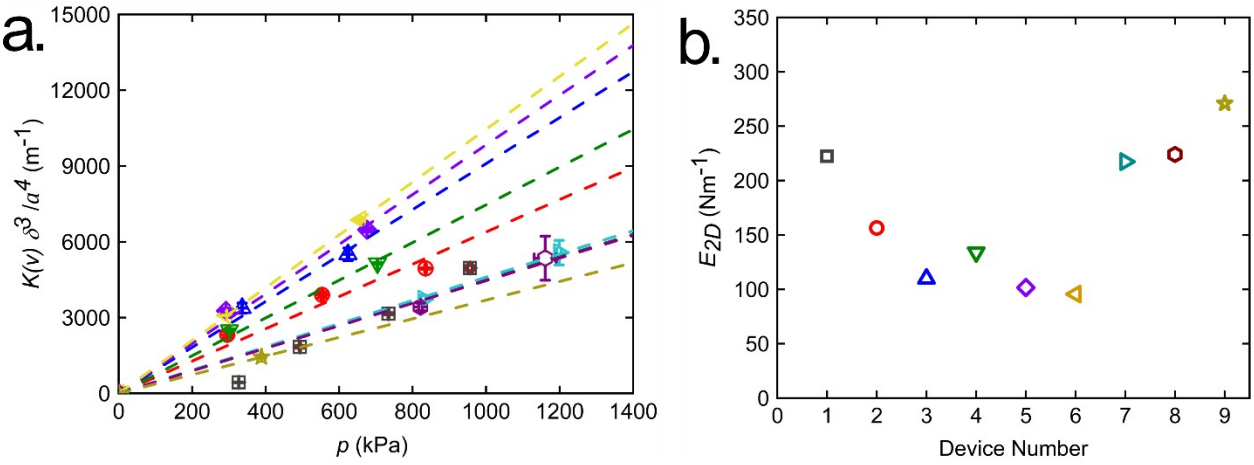

Figure S3. a) $K(v)\delta^3/a^4$ vs p for CVD-grown MoS_2 membranes. Dashed lines are the linear fits used to determine the E_{2D} of each device. **b)** E_{2D} for each device in (a).

4. Shear Modulus Derivation and Free Energy Model

To compute the shear modulus of the FLG, we utilize the governing equations developed by Williams[12] for an axisymmetric membrane, incorporating a shear stress term. The governing equations derived from a force balance in the radial (Figure S4) and transverse directions for this system are:

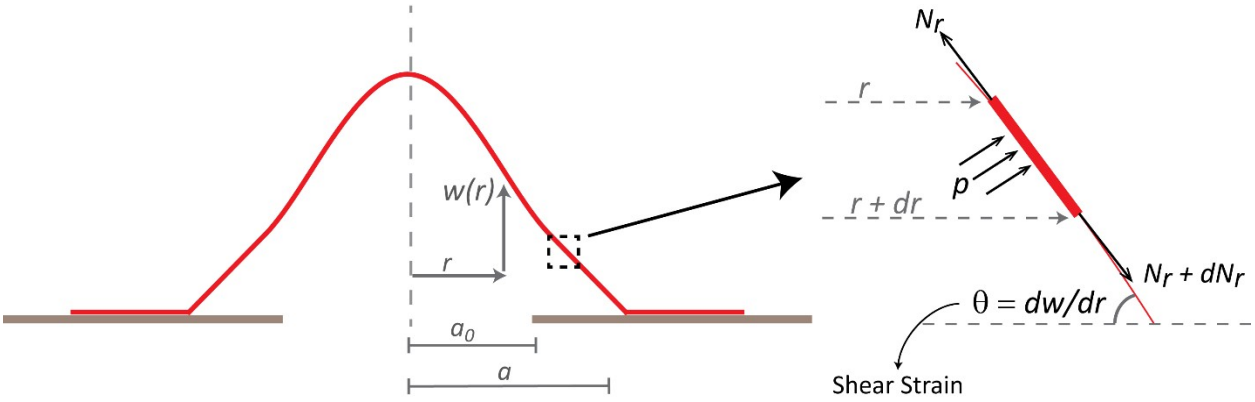

Figure S4. Schematic diagram of the force balance in the radial direction.

$$\frac{d}{dr}(r\,N_r) = N_t \tag{S4.1a}$$

$$\frac{d}{dr}\left(r(N_r + G_{2D})\frac{dw}{dr}\right) = -pr \tag{S4.1b}$$

$$\varepsilon_r = \frac{du}{dr} + \frac{1}{2}\left(\frac{dw}{dr}\right)^2 \tag{S4.2a}$$

$$\varepsilon_t = \frac{u}{r} \tag{S4.2b}$$

$$Et\varepsilon_r = N_r - \nu N_t \tag{S4.3a}$$

$$Et\varepsilon_t = N_t - \nu N_r \tag{S4.3b}$$

where r is the radial coordinate, u is radial displacement, w is transverse deflection, p is the pressure difference, and E, t, ν are the bulk Young's modulus, thickness, and Poisson's ratio of the membrane, respectively. N_r and ε_r are the radial stress and strain, and N_t and ε_t are the circumferential stress and strain. G_{2D} is the two-dimensional shear modulus. G_{2D} is equal to the bulk shear modulus multiplied by the thickness of the layered structure (LS) ($G * (LS\ thickness) = G_{2D}$ (N/m)). Equations S4.1a, b, S4.2a, b, and S4.3a, b can be combined to give:

$$(N_r + G_{2D})^2 \frac{d}{dr}\left(r^3 \frac{dN_r}{dr}\right) = -\frac{Etp^2}{8} r^3 \tag{S4.4}$$

This non-linear equation has been solved using a series approximation for the non-dimensional stress $f = (Etp^2a^2/64)^{-1/3} (N_r+G_{2D})$. As a result, Eqn. S4.4 can be non-dimensionalized as ($\zeta = r/a$):

$$f^2 \frac{d}{d\zeta}\left(\zeta^3 \frac{df}{d\zeta}\right) = -8\,\zeta^3 \tag{S4.5}$$

Furthermore, we sub-divide the whole blister into two regions along the radial direction: (i) Region I ($r \le a_0$) is where only MoS_2 is suspended and (ii) Region II ($a_0 < r \le a$) is area outside the microcavity which forms the MoS_2/FLG LS. Therefore, the non-dimensional stress can be written in series forms as:

$$f_i = \sum_{l=0,1,\ldots} A_{i(2l)} \zeta^{2l} = \begin{cases} Region\ I & (r \le a_0) & i = 1 \\ Region\ II & (a_0 < r \le a) & i = 2 \end{cases} \tag{S4.6}$$

We substitute Eqn. S4.6 into Eqn. S4.5 and equating terms on both sides we obtain $A_{i2} = -1/(A_{i0})^2$, $A_{i4} = -2/(3A_{i0}^5)$, $A_{i6} = -13/(18A_{i0}^8)$, $A_{i8} = -17/(18A_{i0}^{11})$, $A_{i10} = -37/(27A_{i0}^{14})$, $A_{i12} = -1205/(567A_{i0}^{17})$, … etc.

For the deflection profile *w(r)* of the delaminated LS device, we carry out the same regional approach which results in:

$$w(r) = \begin{cases} w_1(r) = \left(\frac{pa^4}{Et}\right)^{\frac{1}{3}} \sum_{j=0,1,\ldots} C_j \zeta^{2j}\ , & Region\ I\ (r \le a_0) \\ w_2(r) = \left(\frac{pa^4}{Et}\right)^{\frac{1}{3}} \sum_{j=0,1,\ldots} B_j (1-\zeta^{(2j+2)}), & Region\ II\ (a_0 < r \le a) \end{cases}$$

(S4.7)

First, we obtain C_j and B_j by equating terms with the same exponent of r on both sides of the non-dimensionalized Eqn. S4.1b while using the series expression for the non-dimensional stress function, f as defined in Eqn. S4.6. As a result, C_j is written in terms of A_{10} such that $C_2 = -1/A_{10}$, $C_4 = -1/(2A_{10}^4)$, $C_6 = -5/(9A_{10}^7)$, $C_8 = -55/(72A_{10}^{10})$, $C_{10} = -7/(6A_{10}^{13})$, …, etc., and B_i in terms of A_{20} such that $B_0 = 1/A_{20}$, $B_2 = 1/(2A_{20}^4)$, $B_4 = 5/(9A_{20}^7)$, $B_6 = 55/(72A_{20}^{10})$, $B_8 = 7/(6A_{20}^{13})$, $B_{10} = 205/(108A_{20}^{16})$, …, etc. Next, we determine A_{20} by utilizing the fixed boundary condition $u(r = a) = 0$ for region II which results in:

$$\frac{d}{d\zeta}(\zeta f_2) - \upsilon f_2 = (1-\nu) f_0 \qquad \text{(S4.8)}$$

where $f_0 = 4G_{2D}/(Etp^2a^2)^{1/3}$. Subsequently, A_{10} can be obtained by using the governing equation and continuity condition $u(r = a_{0-}) = u(r = a_{0+})$ which results in:

$$\frac{d}{d\zeta}(\zeta f_2) - \upsilon f_2 - (1-\nu) f_0 = \frac{d}{d\zeta}(\zeta f_1) - \upsilon f_1 \qquad \text{(S4.9)}$$

Finally, we obtain the remaining unknown C_0 by enforcing the continuity condition $w^-(\zeta = a_0/a) = w^+(\zeta = a_0/a)$.

As the next step, we model the blister as a thermodynamic system. This involves developing a free energy model that comprises four parts.

$$F = F_{mem} + F_{gas} + F_{ext} + F_{adh} \tag{S4.10}$$

F_{mem} refers to the strain energy term resulting from the stretching caused by the application of a pressure load on the membrane. It is expressed as:

$$F_{mem} = \int_0^a \left(\frac{1}{2}\left(N_r\epsilon_r + N_t\epsilon_t\right)\right) 2\pi r dr \; + \int_{a_0}^{a} \frac{1}{2} G_{2D}\left(\frac{dw}{dr}\right)^2 2\pi r dr \tag{S4.11}$$

We divide the integral of the MoS_2 membrane's strain energy contribution due to the stretching (first term in Eqn. S4.11) into two regions and introduce the parameter $\rho = a_0/a$ to non-dimensionalize the expression. We define $U_{strain1}$ is the non-dimensionalized strain energy within the well region ($\rho < a_0/a$), and $U_{strain2}$ is that within the delaminated region of the blister ($a_0/a < \rho < 1$). This results in:

$$U_{Strain1} = \int_0^{\rho} \left((f_1)^2 + \frac{d}{d\zeta}(\zeta f_1)^2\right)\zeta \; d\zeta - \; v\int_0^{\rho} \left(2f_1 \frac{d}{d\zeta}(\zeta f_1)\right)\zeta \; d\zeta \tag{S4.12}$$

$$U_{Strain2} = \int_{\rho}^{1} \left((f_2 - f_0)^2 + \frac{d}{d\zeta}(\zeta(f_2 - f_0))^2\right)\zeta \; d\zeta \; - \; v\int_{\rho}^{1} \left(2(f_2 - f_0)\frac{d}{d\zeta}(\zeta(f_2 - f_0))\right)\zeta \; d\zeta \tag{S4.13}$$

Next, we proceed to evaluate the second term in $F_{mem,}$ which accounts for the shear contribution. We express this term as in its non-dimensionalized form as ($\hat{w} = w\left(\frac{pa^4}{Et}\right)^{-1/3}$ non-dimensionalized deflection):

$$U_{Shear} = \int_{\rho}^{1} \zeta^2 \left(\frac{d\hat{w}}{d\zeta}\right)^2 \pi d\zeta \tag{S4.14}$$

and the final expression for F_{mem} is,

$$F_{mem} = \left(\frac{pa^4}{Et}\right)^{1/3}\left(\frac{\pi\, pa^2}{16}\left(U_{Strain1} + U_{Strain2}\right) + \left(\frac{pa^4}{Et}\right)^{1/3} G_{2D}\, U_{Shear}\right) \tag{S4.15}$$

F_{gas} is the energy change due the expansion of the gas molecules trapped in the blister,

$$F_{gas} = -p_0 V_0\, ln\left(\frac{V_0 + V_b}{V_0}\right) \tag{S4.16}$$

F_{ext} is the energy change of the external environment,

$$F_{ext} = -p_{ext} V_b \tag{S4.17}$$

F_{adh} is the adhesion energy of the LS-substrate interface,

$$F_{adh} = \Gamma\, \pi \left(a^2 - a_0^2\right) \tag{S4.18}$$

where Γ is separation energy per unit area. During the analysis of the free energy, we utilize multiple terms (up to 5 terms) in the non-dimensionalized stress function, f. However, as we add more terms to the series, the computational cost increases. After comparing the results, we observed that beyond the inclusion of 3 terms in the series, there is no significant change, and the results converge to the same approximated value. Therefore, we made the decision to utilize the 3-term expansion, which yields satisfactory results in numerical solutions. With this approach, we plot the input pressure vs. shear modulus for all tested devices in Figure S5. By conducting the blister test at various input pressures, we induce multiple instances of delamination in the devices.

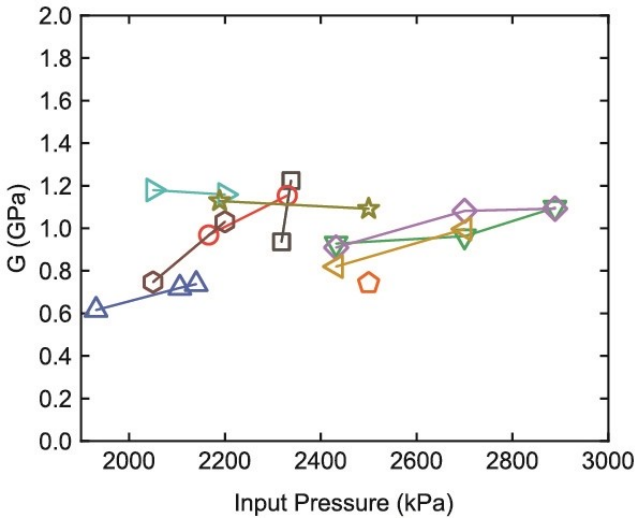

Figure S5. Shear modulus development of each device against varying input pressure. 9 devices undergo multiple delamination from the surface.

5. Investigation of the Delamination Behavior of the LS System by Varying the Thickness

In the experiments, we observed two distinct delamination behaviors across different devices: (i) only the MoS_2 membrane delaminates from the surface of FLG, and (ii) MoS_2/FLG LS delamination from the SiO_x surface. The primary distinction between the devices lies in the varying thickness of the FLG. To comprehend this transition, in Figure S6, we plot the critical pressure (p_{cr}) at which the blister first delaminates vs. the thickness of the LS. Employing the microcavity dimensions (well depth = 600 nm, well radius = 2.5 μm), we calculate the critical pressure ($p_{cr\text{-}Hencky}$), such that only the MoS_2 membrane separating from the FLG, using Hencky's free energy model.[4,13] To calculate the critical pressure, we use the expression:[14]

$$\Gamma_{sep} = \frac{5}{4} C K E_{2D} \left(\frac{\delta}{a}\right)^4 \qquad \text{(S5.1)}$$

First, by rearranging the Eqn. S5.1, we determine the critical deflection just before the delamination occurs (Γ_{sep} = 0.39 J/m^2, C = 0.522, K=3.55, E_{2D}= 180 N/m). Next, we calculate bulge volume (V_b) and obtain p_{int} by using Eqn. S3.1. Finally, we substitute these values back into ideal gas law to find the $p_{cr\text{-}Hencky}$. Additionally, we plot the critical pressure ($p_{cr\text{-}LS}$) for MoS_2/FLG LS delamination from the SiO_x surface in Figure S6. To do this, we numerically solve the LS model we developed by incorporating the calculated mean G value (G = 0.97 GPa) as well as values, G = 1.12 and 0.82 GPa, that are one standard deviation from the calculated mean G value. This helps us establish the range within which $p_{cr\text{-}LS}$ corresponds to the pressure just before the diameter expansion occurs. See main text for the parameters used in the calculation. Based on the intersection of $p_{cr\text{-}Hencky}$ and $p_{cr\text{-}LS}$ we define 2 zones: (i) Zone #1 includes the region up to the intersection of $p_{cr\text{-}LS}$ (G = 0.82 GPa) and $p_{cr\text{-}Hencky}$ where we observe delamination of LS, (ii) Zone #2 encompasses the region starting from intersection of the $p_{cr\text{-}LS}$ (G = 1.12 GPa) and $p_{cr\text{-}Hencky}$. The hatched area is what we call the transition zone, where we observe both LS (MoS_2/FLG) and regular (only MoS_2) delamination. In this region, the free energy curves (see the main text) from the LS model and Hencky's model reach their equilibrium configuration (dF/da = 0) at very similar critical pressures. Thus, small variations in adhesion strength, and surface–LS interaction can lead to either regular or LS delamination when $p_o > p_{cr}$. The intersection point of $p_{cr\text{-}LS}$ (G = 0.82 GPa (red line)) and $p_{cr\text{-}Hencky}$ (dashed line) provides the cutoff thickness below which we expect LS delamination is preferred over MoS_2 separation from FLG. We also populated Figure S6 with two sets of data points: (i) black data points represent devices that exhibit FLG/MoS_2 LS delamination from the SiO_x surface, and (ii) purple data points show regular delamination where only the monolayer MoS_2 membrane separates from the FLG surface.

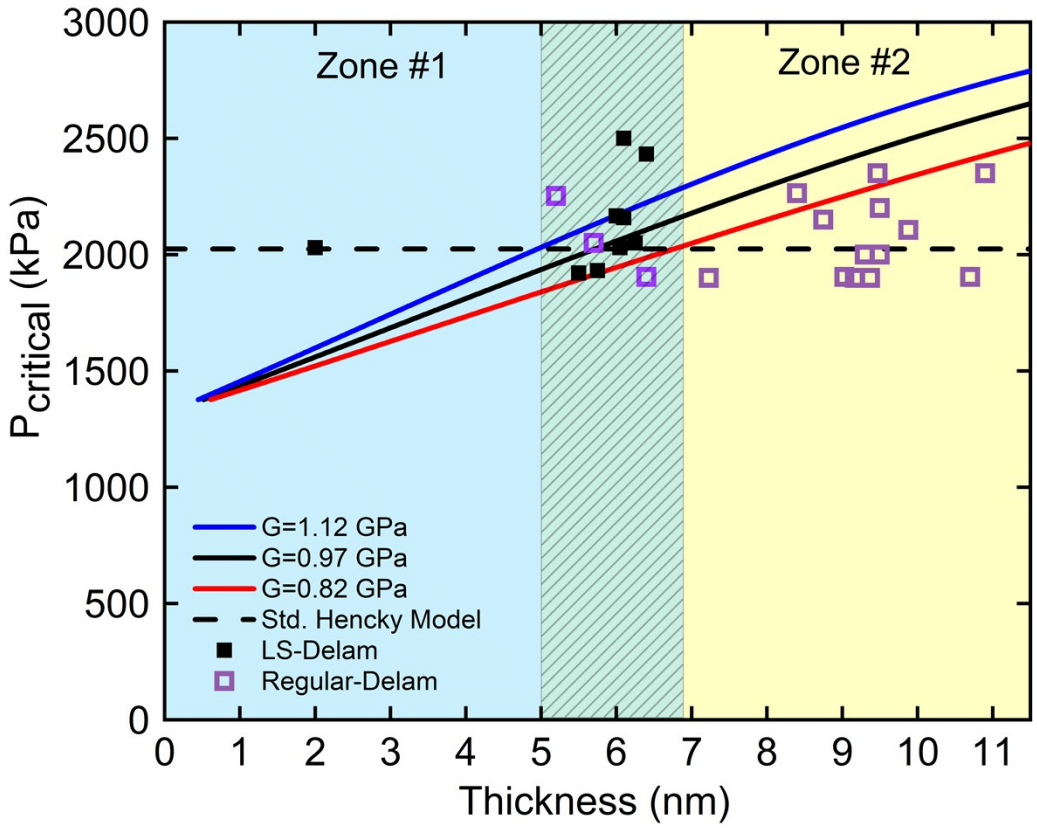

Figure S6. p_{cr} vs thickness of MoS_2/FLG LS device. The solid lines show the expected p_{cr} using the measured average shear modulus (black), plus (blue), and minus (red) one standard deviation. The dashed line is the expected p_{cr} for delamination of MoS_2 from the FLG surface using the standard Hencky's solution. The plot is divided into two zones; (i) Zone #1 where we observe only LS delamination, (ii) Zone #2 where we observe only MoS_2 delamination, and the hatched transition zone where we both.

6. Raman Spectroscopy Analysis over the Delaminated Blister

We performed Raman spectroscopy to verify the delamination of graphite flakes with the MoS_2 membrane. We carry out the scan through points located along the dashed line shown in Figure S7a and sub-divide the line scan into 5 regions. Region 1 (Fig. S7b) and region 5 (Fig. S7f) are on the supported area where there is no delamination. In region 2 (Fig. S7c) and region 4 (Fig. S7e),

we observe LS delamination where both FLG and MoS_2 separated from the surface together and we measure the graphite G and 2D Raman peaks[15], however the intensities are lower compared to the supported area presumably due to interference.[16] In region 3 (Fig. S7d), we have only the MoS_2 membrane suspended over the microcavity. Signals of the 2D peak from FLG disappear and the MoS_2 Raman resonance peaks become more prominent.

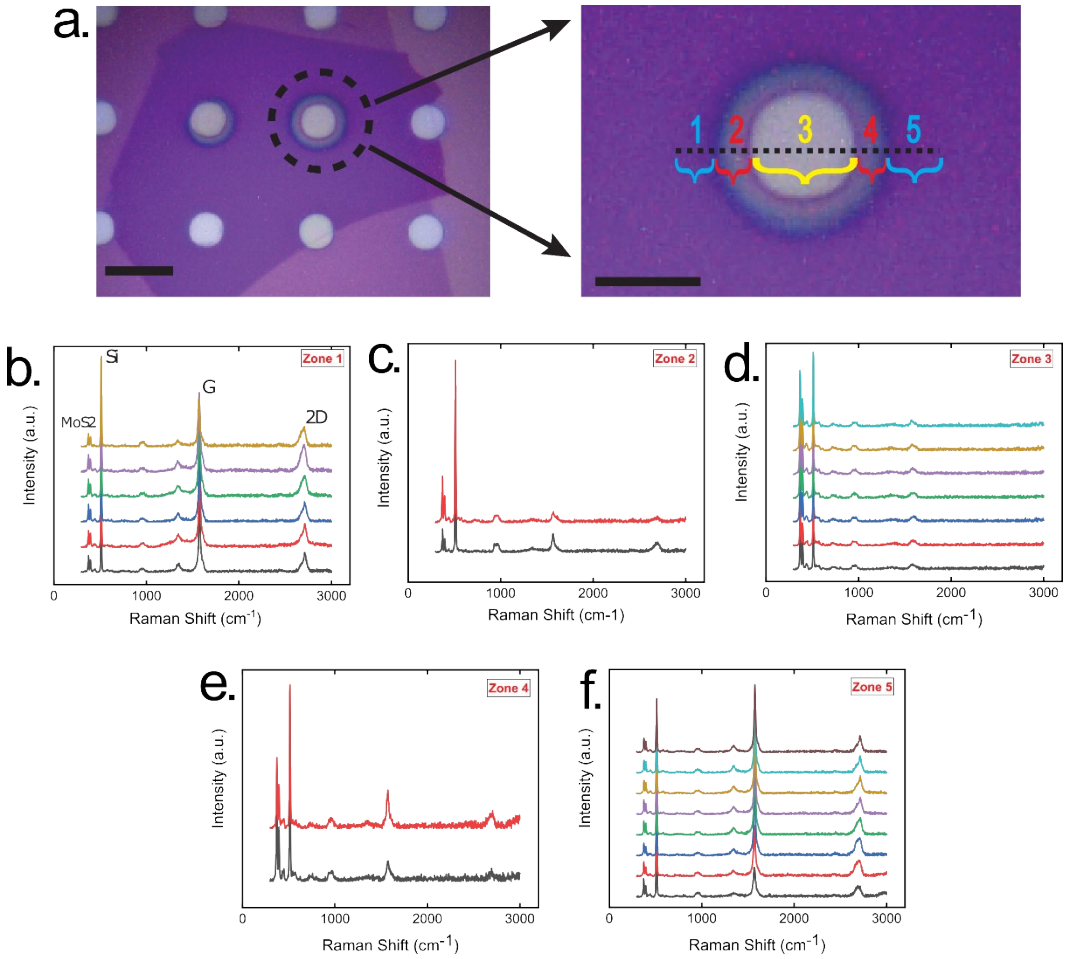

Figure S7. a) Optical image of FLG/MoS_2 which shows LS delamination labeled with a circled dash line. The scale bar is 10 μm (Left image). Raman spectroscopy is carried out over points which lie on the dashed line (Right image – Scale bar is 5 μm) We sub-divided Raman spectrum into 5 regions. **b)** and **f)** are Raman spectrum over the supported area with no delamination. In (b), we labeled the peaks correspond to few-layer graphene (G and 2D), Si, and MoS_2. **c)** and **e)** are Raman spectrum over the FLG/MoS_2 with LS delamination. **d)** Raman spectrum over the microcavity where only MoS_2 is suspended.

7. Estimation of Bending Strain Energy

As the thickness of the graphite increases in the LS devices, bending strain energy also needs to be considered in the free energy calculation. To ascertain the necessity of this addition, we begin by determining the bending modulus applicable to our tested devices. Since the LS is primarily composed of few-layer graphene, we used the bending rigidity of graphene in our bending strain energy estimates and used the assumptions of classical plate theory where:

$$D = \frac{E\,h^3}{12\,(1-\nu^2)} \tag{S7.1}$$

where E is Young's modulus, h is the thickness and ν is the Poisson's ratio.

For a 6nm thick (~ 17 layers of graphene) LS case, we calculate a bending rigidity of 1.97 x 10^{-14} J.

The strain energy contribution due to bending by exploiting the expression formularized by Timoshenko[17,18] yields:

$$U_{bending} = D\pi \int_a^{a_0} \left[\left(\frac{d^2w}{dr^2} + \frac{1}{r}\frac{dw}{dr} \right)^2 - 2\,(1-\nu) \left(\frac{d^2w}{dr^2}\frac{1}{r}\frac{dw}{dr} \right) \right] r\,d\theta\,dr \tag{S7.2}$$

For deflection $w(r)$, we approximate it by using the expression:

$$w(r) \approx \frac{a^2 - r^2}{2R} \tag{S7.3}$$

where R is the radius of the curvature. As a result, the bending strain energy estimate is:

$$U_{bending} = \frac{\pi D\,(1+v)}{R^2}\left(a^2 - a_0^2\right) \tag{S7.4}$$

From equation S7.4, we calculate and tabulate results of the bending strain energy and shear strain energy for the 3 tested devices in Table S1.

	Input Pressure(p_0) (kPa)	Shear Strain Energy (J)	Bending Strain Energy (J)	Thickness (nm)
Device ID: Q_W23	2318	2.80×10^{-12}	2.50×10^{-15}	6.25
Device ID: C2_S18	2166	1.71×10^{-12}	1.83×10^{-15}	6
Device ID: AH_X29	2106	3.98×10^{-12}	3.19×10^{-15}	5.75

Table S1. Comparison of calculated strain energy contributions for 3 tested devices.

It can be seen that bending strain energy is 3 orders of magnitude less than the shear strain energy in this thickness range. Therefore, we omit the contribution of bending from the free energy model.

8. Thickness Dependence of the LS Delamination Profile

In Figure S6, it can be observed that the devices which show LS delamination mostly lie within the 5 nm to 7 nm thickness range. The main reason is that when the combined thickness (thickness of MoS_2 + thickness of few-layer graphene) is below 5 nm, the LS delamination becomes hard to distinguish from a regular delamination in the AFM profile. To illustrate this, using the same device parameters (radius and depth) and G = 0.97 GPa, we plot the delaminated profile of the blisters at critical pressure as a function of varying device thickness in Figure S8. When the FLG

thickness is zero ($f_0 = 0$), the result of the LS model matches that of Hencky's free energy model (dashed line in Figure S8).

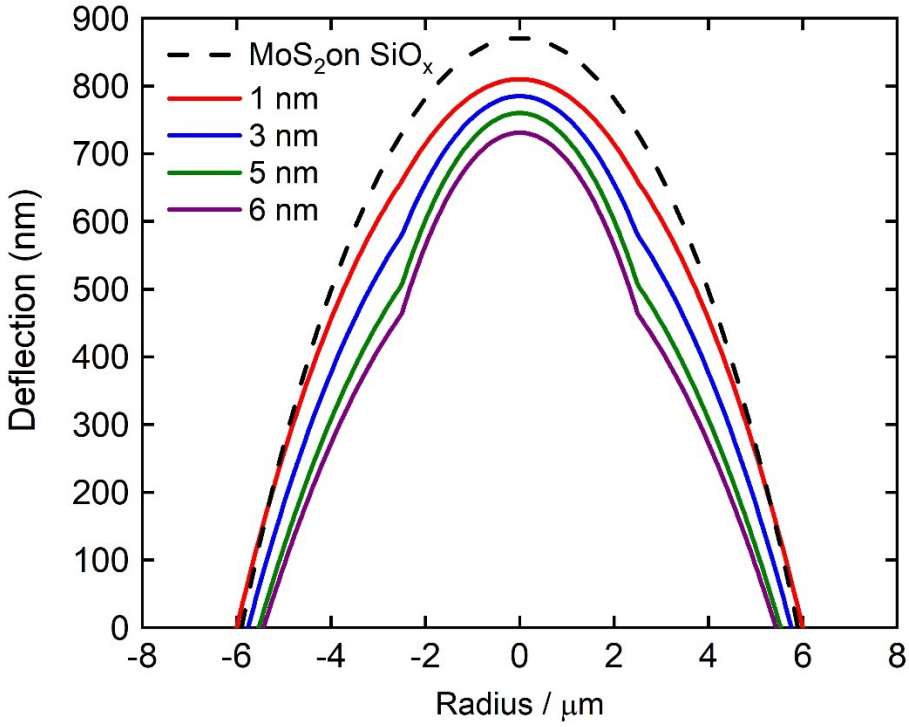

Figure S8. Profile change correspondences to varying combined thickness of LS.

9. Non-Circular Delamination Example

In our experiments, we also observe asymmetric/non-axisymmetric delamination of MoS_2/FLG LS from the SiO_x surface. In Figure S9 and S10, we show AFM amplitude images from two different devices. Before delamination, the MoS_2 bulges stay axisymmetric, and at higher pressures, the MoS_2/FLG begins to delaminate from the surface. The LS delamination occurs radially outward in a preferred direction. We attribute this to possible surface inhomogeneities around the blister[19], or structural defect.[20,21]

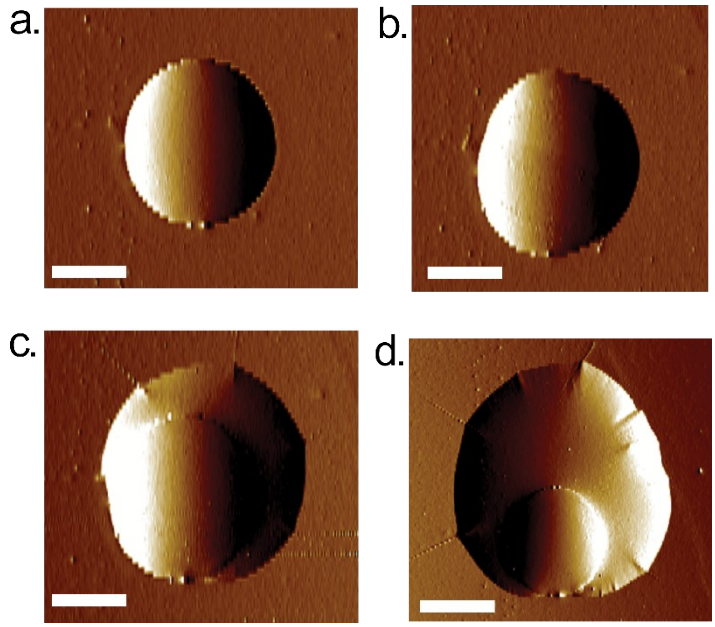

Figure S9. AFM amplitude image of device #1 with non-circular delamination. **a)** at input pressure (p_0) = 1609 kPa **b)** at p_0=1780 kPa **c)** at p_0= 2325 kPa **d)** at p_0= 3634 kPa. Scale bars are 2.5 μm.

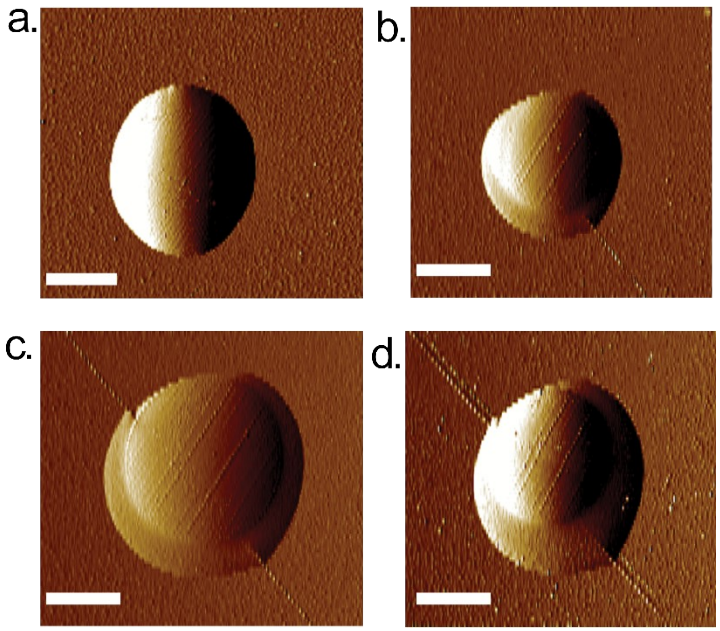

Figure S10. AFM amplitude image of device #2 with non-circular delamination. **a)** at p_0= 1300 kPa **b)** at p_0 =1588 kPa **c)** at p_0=1620 kPa **d)** at p_0=1906 kPa. Scale bars are 2.5 μm.

We also observe MoS_2/FLG undergoing dramatic delamination when two devices are in close proximity and coalescing together resulting in a very large and irregular-shaped blister (Fig. S11 and Fig. S12).

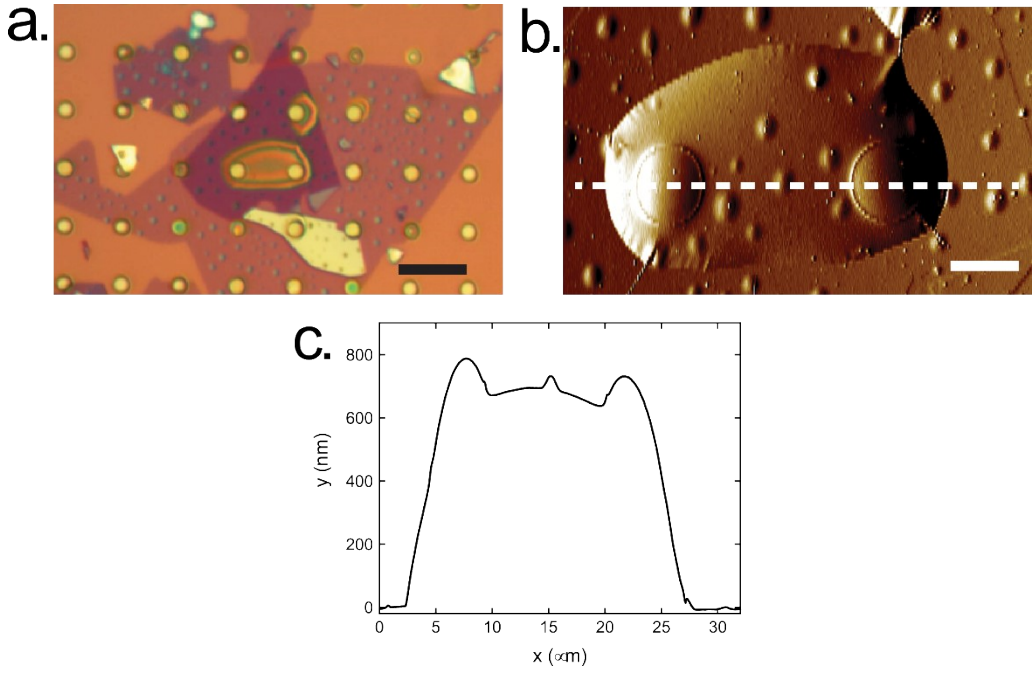

Figure S11. a) Optical image (Scale bar is 20 μm) and **b)** AFM amplitude image (Scale bar is 5 μm) of two blisters coalesced together. **c)** Deflection profile of the large delaminated configuration which is labeled with a dashed line in (b).

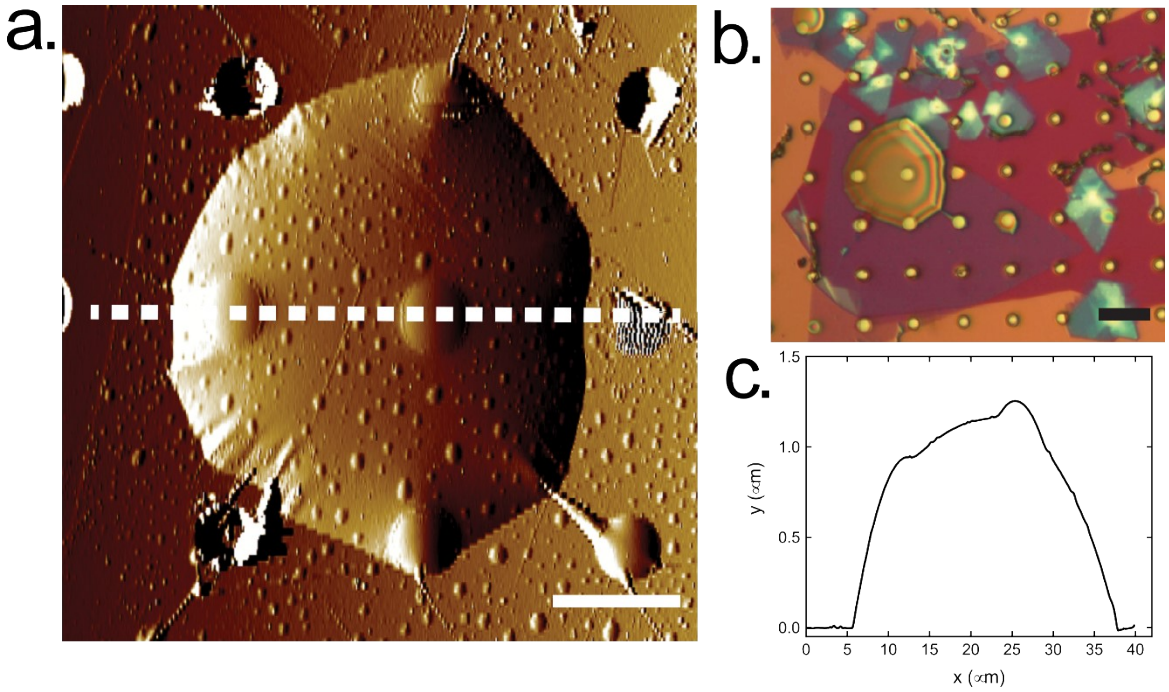

Figure S12. a) AFM amplitude image (Scale bar is 10 μm) and **b)** Optical image (Scale bar is 20 μm) of two blisters coalesced together. **c)** Deflection profile of the large delaminated configuration which is labeled with a dashed line in (a).

References

(1) Luo, G.; Zhang, Z. Z.; Li, H. O.; Song, X. X.; Deng, G. W.; Cao, G.; Xiao, M.; Guo, G. P. Quantum Dot Behavior in Transition Metal Dichalcogenides Nanostructures. *Front. Phys. 2017 124* **2017**, *12* (4), 1–13. https://doi.org/10.1007/S11467-017-0652-3.

(2) Li, F.; Huang, T. De; Lan, Y. W.; Lu, T. H.; Shen, T.; Simbulan, K. B.; Qi, J. Anomalous Lattice Vibrations of CVD-Grown Monolayer MoS2 Probed Using Linear Polarized Excitation Light. *Nanoscale* **2019**, *11* (29), 13725–13730. https://doi.org/10.1039/C9NR03203G.

(3) Mak, K. F.; Lee, C.; Hone, J.; Shan, J.; Heinz, T. F. Atomically Thin MoS2: A New Direct-Gap Semiconductor. *Phys. Rev. Lett.* **2010**, *105* (13), 136805. https://doi.org/10.1103/PhysRevLett.105.136805.

(4) Boddeti, N. G.; Koenig, S. P.; Long, R.; Xiao, J.; Bunch, J. S.; Dunn, M. L. Mechanics of Adhered, Pressurized Graphene Blisters. *J. Appl. Mech. Trans. ASME* **2013**, *80* (4). https://doi.org/10.1115/1.4024255.

(5) Fichter, W. B. Some Solutions for the Large Deflections of Uniformly Loaded Circular Membranes. *NASA Tech. Pap.* **1997**, *3658*, 1–24.

(6) Lloyd, D.; Liu, X.; Boddeti, N.; Cantley, L.; Long, R.; Dunn, M. L.; Bunch, J. S. Adhesion, Stiffness, and Instability in Atomically Thin MoS2 Bubbles. *Nano Lett.* **2017**, *17* (9), 5329–5334. https://doi.org/10.1021/ACS.NANOLETT.7B01735.

(7) Cooper, R. C.; Lee, C.; Marianetti, C. A.; Wei, X.; Hone, J.; Kysar, J. W. Nonlinear Elastic Behavior of Two-Dimensional Molybdenum Disulfide. *Phys. Rev. B - Condens. Matter Mater. Phys.* **2013**, *87* (3), 035423. https://doi.org/10.1103/PhysRevB.87.035423.

(8) Hong, J.; Hu, Z.; Probert, M.; Li, K.; Lv, D.; Yang, X.; Gu, L.; Mao, N.; Feng, Q.; Xie, L.; Zhang, J.; Wu, D.; Zhang, Z.; Jin, C.; Ji, W.; Zhang, X.; Yuan, J.; Zhang, Z. Exploring Atomic Defects in Molybdenum Disulphide Monolayers. *Nat. Commun. 2015 61* **2015**, *6* (1), 1–8. https://doi.org/10.1038/ncomms7293.

(9) Gan, Y.; Zhao, H. Chirality Effect of Mechanical and Electronic Properties of Monolayer MoS2 with Vacancies. *Phys. Lett. A* **2014**, *378* (38–39), 2910–2914. https://doi.org/10.1016/J.PHYSLETA.2014.08.008.

(10) Zandiatashbar, A.; Lee, G. H.; An, S. J.; Lee, S.; Mathew, N.; Terrones, M.; Hayashi, T.; Picu, C. R.; Hone, J.; Koratkar, N. Effect of Defects on the Intrinsic Strength and Stiffness of Graphene. *Nat. Commun. 2014 51* **2014**, *5* (1), 1–9. https://doi.org/10.1038/ncomms4186.

(11) Liu, B.; Pavlou, C.; Wang, Z.; Cang, Y.; Galiotis, C.; Fytas, G. Determination of the Elastic Moduli of CVD Graphene by Probing Graphene/Polymer Bragg Stacks. *2D Mater.* **2021**, *8* (3), 035040. https://doi.org/10.1088/2053-1583/ABFEDB.

(12) Williams, J. G. Energy Release Rates for the Peeling of Flexible Membranes and the Analysis of Blister Tests. *Int. J. Fract.* **1997**, *87* (3), 265–288. https://doi.org/10.1023/A:1007314720152.

(13) Koenig, S. P.; Boddeti, N. G.; Dunn, M. L.; Bunch, J. S. Ultrastrong Adhesion of Graphene Membranes. *Nat. Nanotechnol.* **2011**, *6* (9), 543–546. https://doi.org/10.1038/NNANO.2011.123.

(14) Calis, M.; Lloyd, D.; Boddeti, N.; Bunch, J. S. Adhesion of 2D MoS2 to Graphite and Metal Substrates Measured by a Blister Test. *Nano Lett.* **2023**, *23* (7), 2607–2614. https://doi.org/10.1021/ACS.NANOLETT.2C04886.

(15) Malard, L. M.; Pimenta, M. A.; Dresselhaus, G.; Dresselhaus, M. S. Raman Spectroscopy in Graphene. *Phys. Rep.* **2009**, *473* (5–6), 51–87. https://doi.org/10.1016/J.PHYSREP.2009.02.003.

(16) Li, S. L.; Miyazaki, H.; Song, H.; Kuramochi, H.; Nakaharai, S.; Tsukagoshi, K. Quantitative Raman Spectrum and Reliable Thickness Identification for Atomic Layers on Insulating Substrates. *ACS Nano* **2012**, *6* (8), 7381–7388. https://doi.org/10.1021/NN3025173.

(17) Timoshenko, S.; Woinowsky-Krieger, S. *Theory of Plates and Shells*; McGraw-Hill,: New York, 1959.

(18) Reddy, J. N. *Theories and Analyses of Beams and Axisymmetric Circular Plates*, 1st ed.; CRC Press: Boca Raton, 2022. https://doi.org/10.1201/9781003240846.

(19) Lee, J.; Lee, N.; Lansac, Y.; Jang, Y. H. Charge Inhomogeneity of Graphene on SiO2: Dispersion-Corrected Density Functional Theory Study on the Effect of Reactive Surface Sites. *RSC Adv.* **2014**, *4* (70), 37236–37243. https://doi.org/10.1039/C4RA06499B.

(20) Banhart, F.; Kotakoski, J.; Krasheninnikov, A. V. Structural Defects in Graphene. *ACS Nano* **2011**, *5* (1), 26–41. https://doi.org/10.1021/NN102598M.

(21) Yang, G.; Li, L.; Lee, W. B.; Ng, M. C. Structure of Graphene and Its Disorders: A Review. *Sci. Technol. Adv. Mater.* **2018**, *19* (1), 613. https://doi.org/10.1080/14686996.2018.1494493.